Combining optical and radar satellite image time series to map natural vegetation: savannas as an example

Mailys Lopes, Pierre-Louis Frison, Sarah.M. Durant, Henrike Schulte To Bühne, Audrey Ipavec, Vincent Lapeyre, Nathalie Pettorelli

Remote Sensing in Ecology and Conservation
Open Access
ZSL LET'S WORK FOR WILDLIFE

ORIGINAL RESEARCH

Combining optical and radar satellite image time series to map natural vegetation: savannas as an example

Mailys Lopes[1,2,3], Pierre-Louis Frison[3], Sarah M. Durant[1], Henrike Schulte to Bühne[1], Audrey Ipavec[1], Vincent Lapeyre[4] & Nathalie Pettorelli[1]

[1]Institute of Zoology, Zoological Society of London, London, United Kingdom
[2]DYNAFOR, University of Toulouse, INRA, Castanet-Tolosan, France
[3]LaSTIG, Université Paris Est, IGN, Marne-la-Vallée, France
[4]Conservation Programmes, Zoological Society of London, London, United Kingdom

Keywords
Data combination, natural vegetation classification, satellite image time series, savanna, Sentinel-1, Sentinel-2

Correspondence
Nathalie Pettorelli, Institute of Zoology, Zoological Society of London, London, UK.
Email: nathalie.pettorelli@ioz.ac.uk

Editor: Ned Horning

Received: 10 June 2019; Revised: 21 November 2019; Accepted: 22 November 2019

doi: 10.1002/rse2.139

Abstract

Up-to-date land cover maps are important for biodiversity monitoring as they are central to habitat and ecosystem distribution assessments. Satellite remote sensing is a key technology for generating these maps. Until recently, land cover mapping has been limited to static approaches, which have primarily led to the production of either global maps at coarse spatial resolutions or geographically restricted maps at high spatial resolutions. The recent availability of optical (Sentinel-2) and radar (Sentinel-1) satellite image time series (SITS) which provide access to high spatial and very high temporal resolutions, is a game changer, offering opportunities to map land cover using both temporal and spatial information. These data moreover open interesting perspectives for land cover mapping based on data combination approach. However, the usefulness of combining dense time series (more than 30 images per year) and data combination approaches to map natural vegetation has so far not been assessed. To address this gap, this contribution tests the idea that the combined consideration of optical and radar data combination and time series analyses can significantly improve natural vegetation mapping in the Pendjari National Park, a Sahelian savanna protected area in Benin. Results highlight that the combination of Sentinel-1 and Sentinel-2 SITS performs as well as Sentinel-2 SITS alone in terms of classification accuracy. Land cover maps are however qualitatively better when considering the data combination approach. Our results also clearly show that the use of dense/hypertemporal optical time series significantly improves classification outcomes compared to using multitemporal only a few images per year) or monotemporal data. Altogether, this work thus demonstrates the ability of dense SITS to improve discrimination of natural vegetation types using information on their phenology, leading to more detailed and more reliable maps for environmental management.

Introduction

We are facing an unprecedented decline in global biodiversity, yet we currently lack reliable information on the extent and speed of decline in many ecosystems. Such information is needed by decision-makers and practitioners in order to mobilize political action to halt and mitigate against declines. The horizontal structure of ecosystems (which e.g. refers to the level of spatial heterogeneity in a given ecosystem) is an important component of ecosystem assessment, and can be assessed using information on land cover, which itself is considered by many as an important 'essential biodiversity variable' (Skidmore et al. 2015). Satellite remote sensing has become an indispensable tool for monitoring land cover and land cover change as it provides repetitive and standardized measures that are spatially continuous and comparable over time (Nagendra 2001).

Mapping of land cover is generally done either at a broad geographical scale with high temporal but coarse to medium spatial resolution imagery (MODIS, Landsat) or at a small geographical scale with low temporal but very high spatial resolution imagery. This means that land cover mapping is generally either limited to a coarse spatial resolution or to a temporally fixed and geographically restricted approach (Mairota et al. 2015; Gómez et al. 2016). Interestingly, the use of satellite image time series (SITS) has shown to be particularly useful for vegetation mapping, because of its ability to take into account plant phenology (Lambin and Linderman 2006; Duro et al. 2007; Kuenzer et al. 2014). However, because of the common trade-off between spatial and temporal resolutions characterizing land cover mapping approaches, most existing classifications have been, and still are, based on single-date image or cloud-free composite (Li et al. 2011; Peterson and Nelson 2014; White et al. 2014; Gómez et al. 2016).

The launch of new generation satellites – such as the Sentinel suite of satellites, as well as fleets of SmallSats/CubeSats – has recently changed this status quo and could potentially be game changing, offering opportunities to map land cover using high resolution imagery in both the spatial *and* the temporal domains, enabling both the detection of small elements in the landscapes (<30 m × 30 m) and the 'almost in real time' monitoring of vegetation phenology.

For land cover mapping, the temporal information is generally exploited through the extraction of temporal metrics from time series or derived from a model (Schwieder et al. 2016; Chen et al. 2018; Rufin et al. 2019); these metrics do not however account for all existing temporal variations in vegetation phenology.

With the launch of new generation satellites, novel classification protocols and algorithms have emerged to take full advantage of the temporal information contained in dense time series (> 20 images per year) (Inglada et al. 2017; Belgiu and Csillik 2018). However, these new approaches have mostly been applied to crop mapping; the efficiency of dense optical time series to map natural vegetation has so far hardly ever been assessed.

The recent availability of co-registered optical (Sentinel-2) and radar (Sentinel-1) imagery moreover opens promising perspectives for land cover mapping based on a data combination approach, enabling the combined use of the complementary information captured by both types of sensors (Joshi et al. 2016). Fusion or combination of different sources of data can be performed at different stages of the classification. In pre-classification fusion (also known as pixel-level fusion or data-based combination), the different data sources are used together as inputs of the classification algorithm (Joshi et al. 2016). In post-classification fusion (sometimes known as decision-level fusion or result-based combination), classifications obtained from different sources of data are combined to yield a final fused classification (Zhang 2010). A lot of fusion techniques exist and their comparison is not the scope of this paper; reviews of these different fusion techniques can be found in Joshi et al. (2016); Pohl and Genderen (1998); Schulte to Bühne and Pettorelli (2018); and Zhang (2010).

Although optical and radar image fusion have often shown an ability to enhance land cover classification accuracy (Stefanski et al. 2014; Joshi et al. 2016; Clerici et al. 2017), there is still a lack of proper comparison and validation of methods to assess the actual added value of combining optical and radar data for natural vegetation mapping (Gómez et al. 2016; Joshi et al. 2016; Hirschmugl et al. 2018). Although fusion and time series approaches are more and more used, their joint use is still relatively new. Limited availability of imagery has so far limited multitemporal analyses to a few images per year (e.g. Zhu and Tateishi 2006). As a result, little is known about the benefits of combining dense optical and radar SITS for natural vegetation mapping (Kuenzer et al. 2014; Hirschmugl et al. 2018).

To address this knowledge gap, this contribution analyzes the complementarity of radar (Sentinel-1) and optical (Sentinel-2) time series for natural vegetation mapping over a Sahelian savanna protected area in West Africa (in this case the Pendjari National Park). Specifically, we here test the idea that the combination of optical and radar data and dense time series analyses can significantly improve our ability to reliably map natural vegetation, particularly subtle differences in savanna vegetation, providing detailed vegetational maps, including measures of agricultural encroachment, that are needed by managers. Savanna landscapes are important for conservation, being known to host a variety of biodiversity hotspots and key conservation areas (Solbrig 1996). They are characterized by a herbaceous cover with a variable proportion of shrub and woody cover, on a gradient from grasslands to open forests, offering a diversity of habitats for wildlife. This heterogeneity makes savannas difficult to map with satellite images because it leads to pixels composed of a mixture of different land cover types (Eggen et al. 2016). Therefore, land cover classification of savannas has often been limited to a main savanna class encompassing different types of savanna subclasses (such as grass savanna, shrub savanna, tree savanna) (Müller et al. 2015; Eggen et al. 2016; Symeonakis et al. 2018). To our knowledge, the only work that classified savanna following a vegetation height gradient was the contribution of Schwieder et al. (2016) in Brazil using temporal metrics extracted from Landsat time

series; the overall accuracy of their classification was relatively low, at 63%.

Based on the current state of knowledge (Crowson et al. 2019; Hirschmugl et al. 2018; Symeonakis et al. 2018), we expect classifications based on data combination to perform better than classifications based on optical or radar data alone, because data combination takes advantage of the sensitivity of both sensors (H1). Based on previous studies (Archibald and Scholes 2007; Mathieu et al. 2013; Schwieder et al. 2016), we also assume that the differences between close savanna subclasses will rely on small phenological variation. We therefore expect the use of dense time series (here, more than 30 images per year) to significantly enhance land cover classification outcomes compared to single date analysis and multitemporal analysis (six images per year, H2).

Materials and Methods

Study area

The Pendjari National Park is located in the north-west of Benin (Fig. 1A). The park is a component of the W-Arly-Pendjari (WAP) complex which is a large transboundary protected area (36 000 km^2) comprising protected areas in Benin, Burkina Faso and Niger. It is the largest remaining preserved savanna ecosystem in West Africa. The park covers an area of about 2800 km^2,

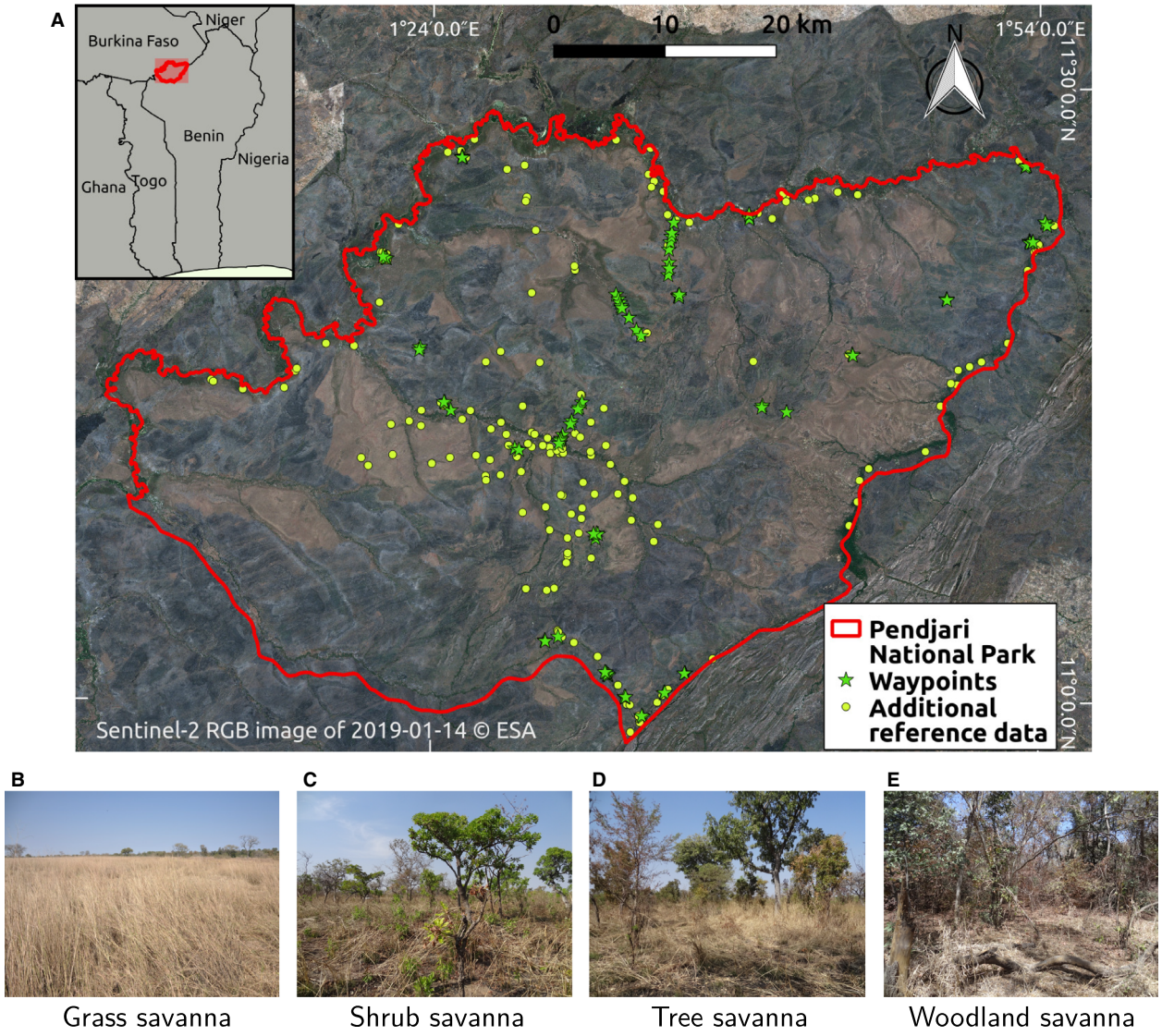

Figure 1. (A) Boundaries of Pendjari National Park with location of reference data and illustrations of the different savanna subclasses (B–E).

subject to a tropical Sudanese-Guinean climate with a rainy season lasting from May to October; average annual precipitation is 1100 mm.

It holds natural habitats that are critical for a number of species, including elephants (*Loxodonta Africana*) (Bouché et al. 2011), the last population of cheetahs in West Africa (*Acinonyx jubatus*) (Durant et al. 2017) and endangered West African lions (*Panthera leo*) (Henschel et al. 2014). It currently is one of the best examples of natural habitats within West Africa.

The boundaries of the Pendjari National Park are almost entirely defined by the Pendjari river that begins in the Atacora mountain chain (formed by hills that have a maximum elevation of 400 m) located in the south of the park. Most of the park is covered by shrub and tree savanna, with wood density getting higher along the Pendjari river and its temporary tributaries, forming riparian and gallery forests. The alluvial plains are mostly covered by grass savanna (Bousquet 1992).

We here consider four savanna subclasses (Fig. 1B–E). Grass savanna is grassland where no ligneous elements are present. Grass can grow up to 2 or 3 m. Shrub savanna is composed of grass and small ligneous elements such as shrubs and bushes that are not higher than 3 m. Tree savanna is composed of grass, shrubs and sparse trees (at least 3 m high) sufficiently spaced so that the leaves of different individuals do not touch each other. Woodland savanna is savanna composed of grass, shrubs and denser tree cover than tree savanna. Leaves can touch each other, especially during wet season when canopy cover is dense. In some nomenclatures, savanna woodland is referred to as clear forest.

Reference data

Ground truth data were collected during a field survey that was carried out in January 2019. About 90 waypoints were recorded across the park using a Global Positioning System (Fig. 1A). Classes that were considered are: grass savanna, shrub savanna, tree savanna, woodland savanna, forest, water bodies, temporary wetlands, bare ground and rocks vegetation. Temporary wetlands were added as an additional category to account for the unique vegetation characteristics of areas that are inundated during the wet season and part of the dry season; in their dry state, they were characterized by bare ground or very low vegetation ground cover. Polygons were then digitized following a small and homogeneous area around the waypoint using Sentinel-2 and Sentinel-1 imagery. Additional small polygons were digitized using knowledge of the local area, information from Google Earth and Sentinel-1 & -2 data, to obtain at least 300 pixels per savanna type.

Satellite imagery

Sentinel-2 is a constellation of two satellites (Sentinel-2A and Sentinel-2B) that carry a MultiSpectral Instrument (MSI) delivering optical images every 5 days. The Pendjari National Park extent is covered by the same Sentinel-2 orbit (R22), therefore, no mosaicking was required. We used the images acquired from 8 February 2018 to 3 February 2019 with less than 50% cloud cover detected on Level L1C products. In total, 43 acquisitions were used. The Level L1C images (orthorectified and radiometrically corrected to Top of Atmosphere reflectance) were processed to Level L2A surface reflectances (corrected for atmospheric effects and slope effects) using the MACCS-ATCOR Joint Algorithm (MAJA) L2A Processor (Hagolle et al. 2010, 2017). The images were downloaded from the PEPS platform of the French Spatial Agency (https://peps.cnes.fr) that allows applying MAJA processor on Sentinel-2 L1C images on the fly. Along with atmospheric and terrain corrections, MAJA processor includes a multi-temporal cloud detector which provides a particularly reliable mask of clouds and cloud shadows (Baetens et al. 2019).

Images acquired by an optical sensor can be affected by the presence of clouds and their shadows resulting in noisy data in the image that should not be considered for classification. When using time series, it results in 'gaps' that do not necessarily occur at the same time for all pixels. For classification purposes, we need to have the same number of dates (i.e. variables) for all the pixels. Therefore, we applied a temporal gap filling algorithm in order to fill the gaps in the time series associated with each pixel. We performed a spline gap filling using the application *Image Time Series Gap Filling* of the Orfeo ToolBox (OTB) which is an open-source toolbox for remote sensing images processing (Grizonnet et al. 2017). We used the ten Sentinel-2 spectral bands at 10 m and 20 m spatial resolution – resampling the six bands at 20 m to 10 m resolution using nearest neighbor interpolation –, as well as the Normalized Difference Vegetation Index (NDVI) (Pettorelli 2013).

Sentinel-1 is a constellation of two satellites with SAR sensors (Sentinel-1A and Sentinel-1B), operating at C-band (5.6 cm wavelength). Over the land surfaces, most acquisitions are made in dual polarization (VV and VH) with a time repeat frequency of 6 days. At the time of the study, only Sentinel-1A acquired images over the Pendjari National Park, providing one acquisition every 12 days. The 31 acquisitions released from 10 February 2018 to 5 February 2019 with the ascending relative orbit 1 were used. This orbit covers 96% of the park with an incident angle varying from 30 to 36°. We used Level-1 Ground Range Detected High resolution (GRDH) products

Table 1. Inputs of the classification

Name	Sensor	Number of dates (variables)		
		Hypertemp.	Multitemp.	Monotemp.
	Sentinel-2			
S2_4	Reflectance in four spectral bands (B2, B3, B4, B8)	43 (172)	6 (21)	1 (4)
S2_10	Reflectance in ten spectral bands (B2, B3, B4, B8, B5, B6, B7, B8A, B11, B12)	43 (430)	6 (60)	1 (10)
S2_4-NDVI	Reflectance in four bands and NDVI	43 (215)	×	×
	Sentinel-1			
S1 _	$\sigma^0_{VH}, \sigma^0_{VV}, \sigma^0_{VH}/\sigma^0_{VV}$	31 (93)	×	×
	Sentinel-1 and Sentinel-2 combination			
S2_4-S1	S2_4 stacked with S1	43 and 31 (265)	×	×
S2_10-S1	S2_10 stacked with S1	43 and 31 (523)	×	×

For the hypertemporal case, all the images of the time series were used. Multitemporal and monotemporal cases were considered for Sentinel-2 only. For the multitemporal case, six dates well distributed in time were extracted from the time series before the gap filling, under the condition that there were 0% cloud cover estimated at L2A. We chose dates 08-02-2018, 05-03-2018, 29-04-2018, 19-05-2018, 26-10-2018, 15-12-2018, 24-01-2019. Note that there are no cloud-free acquisitions during the wet season. For the monotemporal case, we used the Sentinel-2 image acquired on 24-01-2019 because it is the closest date to the field survey with 0% cloud cover.

recorded in interferometric wide swath mode. The images were radiometrically calibrated to convert them to radar backscattering coefficient σ^0 using OTB application *SAR Radiometric Calibration* (Laur et al. 2004). These were then orthorectified to correct for the geometric distortions using the OTB application *OrthoRectification* (Small and Schubert 2008). The output spatial resolution is 10 m per pixel. The images were subsequently converted from intensity to the logarithm dB scale. We used both polarizations VH and VV, and the ratio VH/VV was computed as a third polarization, because multi-polarization data have often been shown to improve land cover classification accuracy (Lee et al. 2001; McNairn et al. 2009a). A temporal filter (Bruniquel and Lopes 1997; Quegan and Yu 2001) was used to reduce the speckle effects without degrading the spatial resolution; the efficiency of such filter when compared to single-date filtered images has been previously demonstrated (Ciuc et al. 2001; Trouve et al. 2003; McNairn et al. 2014).

Classification, accuracy assessment and comparisons

We used the Random Forest (RF) classifier, implemented in OTB applications with the following parameters: maximum depth of tree = 25; minimum number of samples in each node = 25; maximum number of trees in the forest = 100. Those parameters were chosen following [Pelletier et al. 2016] recommendations, as a good compromise between classification accuracy and computation time. Different inputs associated with a time dimension (hypertemporal, multitemporal or monotemporal) were considered as inputs of the classification (Table 1). The combination of optical and radar data was performed for the hypertemporal case only, by stacking both hypertemporal time series prior to classification. The classification workflow can be found in Figure 2.

The reference dataset was split randomly into disjoint training (70%) and validating (30%) subsets. The stratified split was performed at the polygon level in order to have an independent set of pixels between the training and the validation steps (no pixels belonging to the same polygon in the training and validating subsets). The random split was repeated 20 times to ensure the results are not biased by a specific combination of training/validating subsets. The same subsets for a given repetition were used for each input, so that the results are fully comparable. The 20 resulting classifications (for each input) were sieved to reduce the salt and pepper effect using the GDAL (GDAL/OGR contributors, 2018) *gdal_sieve*.

For each iteration, the confusion matrix was computed based on the corresponding validation subset and the *F*-score was extracted as a measure of accuracy, which is the harmonic mean between precision and recall (Sasaki 2007).

To compare the performances of each input configuration, we used the *Z*-statistics of the Wilcoxon rank-sum test (Wilcoxon 1945) computed between each pair of distributions of 20 *F*-scores. The test was run with the SciPy (Jones et al. 2001) library of Python. We also reported the average processing and computational times for each approach and compared them to the average classification accuracy.

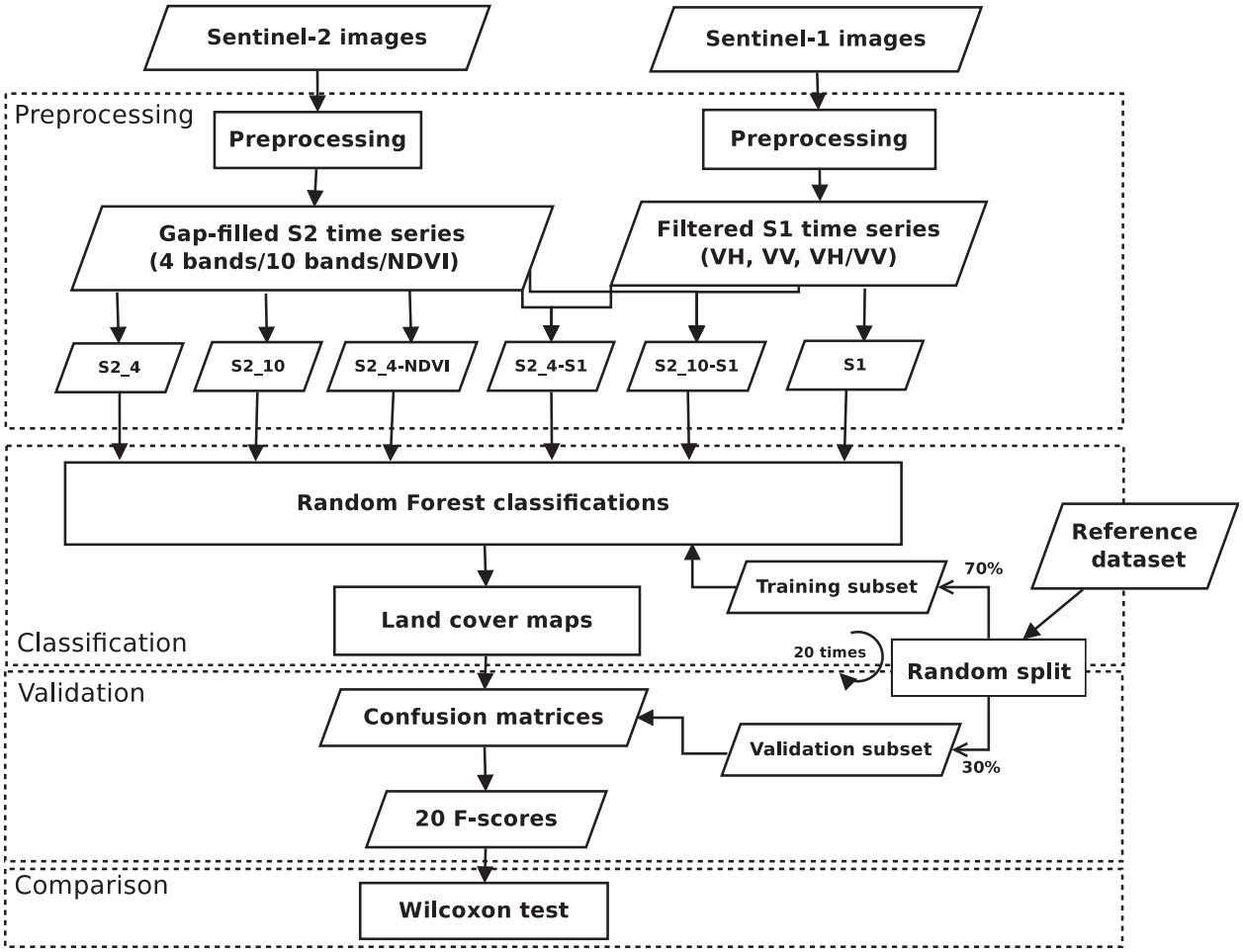

Figure 2. Workflow of the classification scheme.

Results

As expected (H1), the combination of Sentinel-2 and Sentinel-1 SITS provides the highest classification accuracies: the combination of Sentinel-1 with Sentinel-2 (ten bands) or with Sentinel-2 (four bands) leads to equivalent average *F*-scores (respectively 73.2% and 73.0%, Fig. S1). Interestingly, the use of Sentinel-2 SITS alone performs well too, with *F*-scores above 72% using four bands and NDVI or ten bands. Sentinel-1 SITS alone provide the lowest results with an average *F*-score of 60.1%. The results obtained from combining optical and radar data and from Sentinel-2 alone are not significantly different (Table S1).

Overall, the combined use of Sentinel-2 and Sentinel-1 time series leads to forest, water bodies, temporary wetlands, bare ground and rock vegetation being very well classified (per-class *F*-score >90%, Table S2), while grass savanna and woodland savanna are not so well identified (*F*-score > 70%). Our results show that the main confusions are between grass and shrub savanna and between shrub and tree savanna.

On average, shrub savanna is the class that is the most difficult to classify (average *F*-score around 40%, Table S1). Adding Sentinel-1 data to Sentinel-2 data enables a better detection of grass savanna (gain of 4% in accuracy compared to Sentinel-2 alone). Tree savanna is also better detected when adding Sentinel-1 data to Sentinel-2 four bands (gain of 4% in accuracy), but not to Sentinel-2 ten bands (decrease of 4%).

Despite the similar quantitative results given by *F*-score, it is worth noticing that a visual inspection of the produced maps shows a better agreement with the actual landscapes when Sentinel-1 and Sentinel-2 are combined; for example, the narrow lines of trees along temporary streams are much better detected when Sentinel-1 and Sentinel-2 data are combined (Fig. 3C).

As expected (H2), also, the use of a single date clearly leads to poorer classification results (average *F*-score = 52.7% using Sentinel-2 ten bands). Outcomes

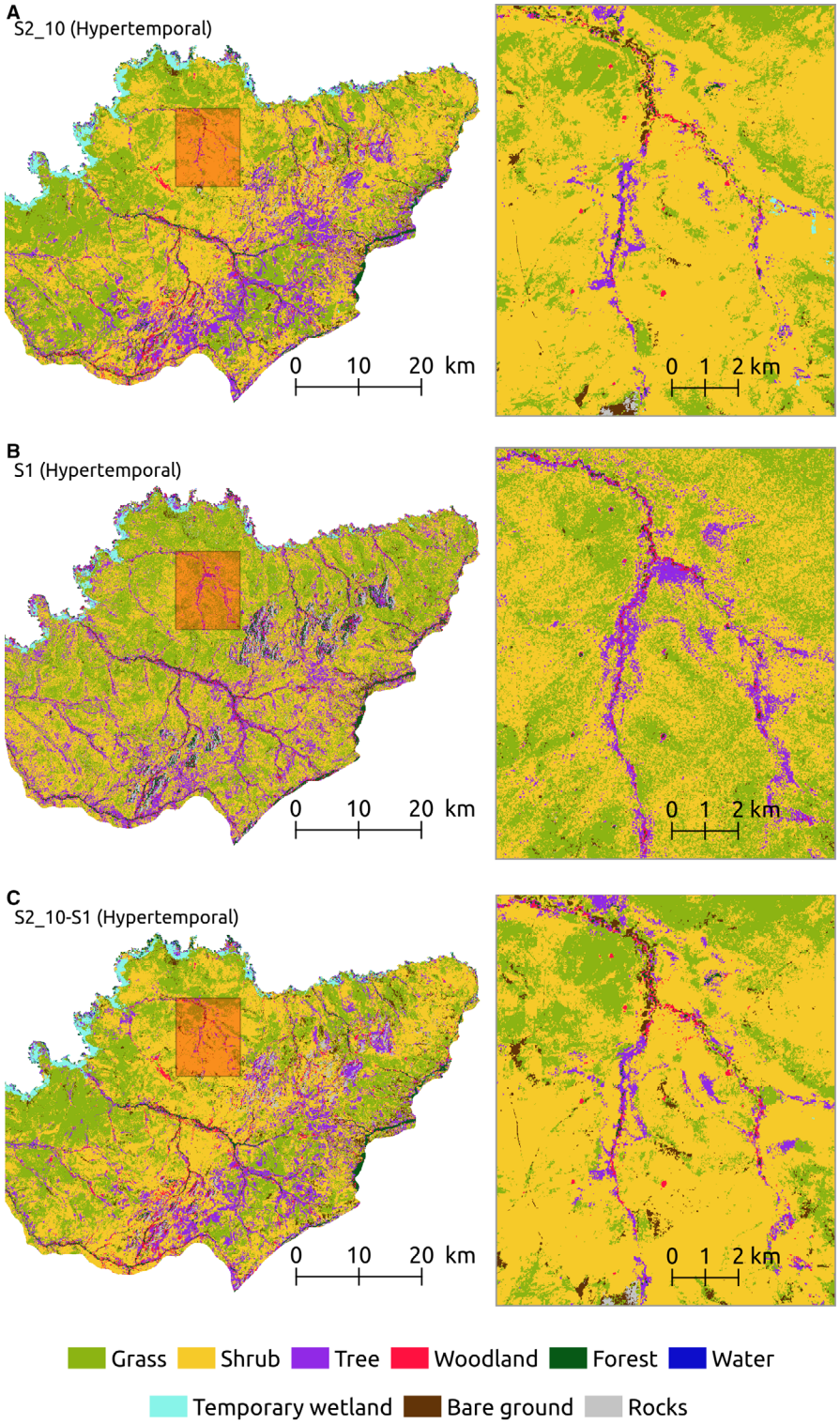

Figure 3. Extract of the hypertemporal classifications using (A) Sentinel-2 data (ten bands) alone, (B) Sentinel-1 data alone and (C) Sentinel-2 combined with Sentinel-1. These are from the same classification iteration, chosen because it has the closest *F*-score to the average *F*-score for the different inputs.

are much improved when using six dates (average *F*-score = 65.3%) but it does not reach the high accuracy obtained using hypertemporal data. The consideration of hypertemporal data results in significantly higher *F*-score than the consideration of multitemporal data (average *F*-score = 72.1%; *P*-value < 0.01 when considering either Sentinel-2 four bands or ten bands).

The added value of using multitemporal or hypertemporal data depends however on the class. For temporally stable classes (forest, water bodies), the gain in accuracy is minor (1% increase at best, Table S2). However, savanna subclasses and classes clearly identifiable by their temporal behavior (temporary wetlands for instance) are much better classified when using hypertemporal data. With Sentinel-2 four bands for example, going from monotemporal to multitemporal data, the gain is of 10% for grass savanna, 9% for shrub savanna, 7% for tree savanna and 37% for woodland savanna. There is an additional gain of 14% for grass savanna, 7% for shrub savanna, 5% for tree savanna when using hypertemporal data (Fig. S2). For temporary wetlands, the gain from monotemporal to multitemporal data is of 44%.

Discussion

Our results demonstrate that the use of hypertemporal optical time series (>30 images per year) can significantly improve land cover mapping in sub-Saharan regions: these findings are in line with those of (Müller et al. 2015; Symeonakis et al. 2018) using Landsat time series. Our results also show for the first time that the combination of both dense Sentinel-1 and Sentinel-2 SITS can potentially enhance classification accuracy, although in our case not significantly. Our validation data, based on field surveys, were sparse and the classification errors might have been larger than the differences in accuracy between both approaches.

Surprisingly, radar time series, although being sensitive to vegetation structure and texture, did not contribute much to improve the discrimination of woody classes; these results contradict the findings of Naidoo and colleagues' work (2016) in which radar data performed better at retrieving woody canopy cover in savannas than Landsat optical data. However, these authors used L-band from ALOS PALSAR which penetrates better in canopy cover than Sentinel-1 C-band. In addition to that, images were acquired in HH/VH polarization; the polarization has an influence on the radar response to vegetation structure (McNairn et al. b) and was shown to impact on the discrimination of woody classes (Mathieu et al. 2013). We did not compare the effect of Sentinel-1 polarizations on the woody classes retrieval, but it could be investigated in future studies. Moreover, as the incident angle of Sentinel-1 is larger than the one of ALOS PALSAR, it could have decreased its ability to distinguish between woody classes because smaller incidence angles are known to penetrate deeper into canopy cover (Inoue et al. 2002). Symeonakis et al. (2018) also found an improved overall accuracy (>5%) when combining optical data (Landsat) and L-band radar data (ALOS PALSAR) for land cover classification in a savanna landscape. These findings suggest that the association of Sentinel-2 with ALOS PALSAR-2 could significantly improve savanna subclasses discrimination. We were not able to test this particular assumption in this study as the 2018 ALOS PALSAR-2 mosaic was not yet available.

One major drawback revealed by our work relates to the use of Sentinel-1 data when working on a spatial extent covered by different orbits. Sentinel-1 has a wide swath of 250 km, with incident angle varying from 30° to 46°. Hence, it is difficult to mosaic Sentinel-1 images acquired over different orbits because overlapping areas are viewed with very different incident angles (Syrris et al. 2019), considerably impacting the magnitude of the backscattered signal as mentioned above (Frison and Mougin 1996; Inoue et al. 2002). To be able to work with different orbits one should have a good distribution of reference data over the different orbits, which is not always easy to obtain especially in conservation areas. In our case, 4% of the parks could not be classified when using Sentinel-1 data because they were covered by a different orbit where we did not have ground truth data. To our knowledge, no study has so far reported this issue because most works involving classification using Sentinel-1 data are set on small geographical extents. Another limitation of this study comes from the combination of optical and radar data that was performed at the pixel-level in a relatively simple way (i.e. only by stacking both types of data prior to classification, resulting in a very high number of input variables). Many fusion techniques exist and could potentially lead to better outcomes when using Sentinel-1 and Sentinel-2 sensors in combination.

Our study has shown that the combined use of dense optical and radar time series has the potential to substantially improve our ability to map natural vegetation in remote areas such as the W-Arli-Penjari transboundary park. However, such an approach is time demanding and requires an advanced set of remote sensing skills. For dense time series pre-processing, on average using a standard computer with 8 Gb RAM and 2.10 GHz × 4 CPU, it took about 45 min to process each full Sentinel-2 time series associated with a 10 m spectral band for the extent of the park, and 1 h 30 for the 20 m spectral bands (an additional step is required, resampling to 10 m). In other

words, 3 hours were required for Sentinel-2 four bands and another 9 h for Sentinel-2 ten bands. For Sentinel-1, 5 h were necessary to obtain the three final filtered time series. In terms of additional computational times during the classification process, it cost about 45 additional seconds to add a supplementary variable to a random forest classification of such an area. At one point, one classification iteration (including model training and image classification) took a total of 1 h 15 for Sentinel-2 four bands, 3 h 30 for Sentinel-2 ten bands, 2 h 30 for the combination of Sentinel-1 and Sentinel-2 four bands and 4 h30 for the combination of Sentinel-1 and Sentinel-2 ten bands. The processing time could be much reduced by using Google Earth Engine platform that provides access to Sentinel imagery and high performance computational infrastructure (Gorelick et al. 2017).

Altogether, this work demonstrates the usefulness of dense SITS to help discriminate among natural vegetation types when mapping land cover. It also highligghts how our reliance on single-date images for land cover mapping limits our ability to monitor ecosystems worldwide, only enabling the distinction of broad classes that are either temporally stable or have a high inter-class separability (such as water, forest, crops, bare ground, built-up areas). Our results thus call for a shift in habits, encouraging a higher use of Sentinel-2 time series to inform environmental management worldwide, particularly in large, conservation relevant regions: although being sensitive to clouds, the high spatial resolution combined to the high revisit frequency of Sentinel-2 appears for example sufficient to map vegetation at fine scale in an area affected by cloud cover, suggesting promising possibilities for land cover classification in tropical areas. Increased use of dense time series will enable a more rapid generation of automatic processing chains with low human intervention, ultimately making tailored land cover mapping more efficient and less sensitive to human errors. For instance, using all the images acquired in a year avoids an arbitrary date selection, often limited by the cloud cover; this approach also allows the use of images acquired during the wet season and subsequently the gap filling of the images (because of clouds) that cannot be done efficiently if using only a few images. Our study shows how such a shift in methodology has the potential to provide more detailed and more reliable maps, that can be used by managers for accurate monitoring of habitat. The approach we detailed is replicable, and only relies on free imagery and open-source software; we therefore hope our results will encourage more scientists and practitioners to consider dense time series analyses as the new norm for tracking changes in the distribution of natural vegetation from space.

Acknowledgments

We thank African Parks, the non-profit conservation organization that manages the Pendjari National Park for allowing us to undertake ground truth data collection in the park. We thank Kiero Marc Ballo and Léni Tandani for accompanying us during data collection and Aurlus Dossia Ouindeyama for his logistic and practical support throughout this field survey.

Data Accessibility

The satellite images used in this study can be downloaded from the PEPS platform of the French Spatial Agency that gives access to the Sentinel products: https://peps.cnes.fr.

The images can be processed using the Orfeo ToolBox open-source software that can be downloaded at https://www.orfeo-toolbox.org.

Funding Information

This publication has been written with the support of the AgreenSkills+ fellowship programme which has received funding from the EU's Seventh Framework Programme under grant agreement N°FP7-609398 (AgreenSkills + contract) and with the support of a Toulouse-INP international mobility grant (SMI).

References

Archibald, S., and R. Scholes. 2007. Leaf green-up in a semi-arid African savanna -separating tree and grass responses to environmental cues. *J. Veg. Sci.* **18**, 583–594.

Baetens, L., C. Desjardins, and O. Hagolle. 2019. Validation of copernicus Sentinel-2 cloud masks obtained from MAJA, Sen2Cor, and FMask processors using reference cloud masks generated with a supervised active learning procedure. *Remote Sens.* **11**, 433.

Belgiu, M., and O. Csillik. 2018. Sentinel-2 cropland mapping using pixel-based and object-based time-weighted dynamic time warping analysis. *Remote Sens. Environ.* **204**, 509–523.

Bouché, P., I. Douglas-Hamilton, G. Wittemyer, A. J. Nianogo, J.-L. Doucet, P. Lejeune, et al. 2011. Will elephants soon disappear from West African savannahs? *PLoS ONE* **6**, 1–11.

Bousquet, B. 1992. Guide des parc nationaux d' Afrique (Afrique du Nord, Afrique de l'Ouest). Delachaux et Niestlé.

Bruniquel, J., and A. Lopes. 1997. Multi-variate optimal speckle reduction in SAR imagery. *Int. J. Remote Sens.* **18**, 603–627.

Chen, Y., D. Lu, E. Moran, M. Batistella, L. V. Dutra, I. D. Sanches, et al. 2018. Mapping croplands, cropping patterns, and crop types using MODIS time-series data. *Int. J. Appl. Earth Obs. Geoinf.* **69**, 133–147.

Ciuc, M., P. Bolon, E. Trouvé, V. Buzuloiu, and J. P. Rudant. 2001. Adaptive-neighborhood speckle removal in multitemporal synthetic aperture radar images. *Appl. Opt.* **40**, 5954–5966.

Clerici, N., C. A. V. Calderón, and J. M. Posada. 2017. Fusion of Sentinel-1A and Sentinel-2A data for land cover mapping: a case study in the lower Magdalena region, Colombia. *J. Maps* **13**, 718–726.

Crowson, M., E. Warren-Thomas, J. K. Hill, B. Hariyadi, F. Agus, A. Saad, et al. 2019. A comparison of satellite remote sensing data fusion methods to map peat swamp forest loss in Sumatra, Indonesia. *Remote Sens. Ecol. Conserv.* **5**, 247–258.

Durant, S. M., N. Mitchell, R. Groom, N. Pettorelli, A. Ipavec, A. P. Jacobson, et al. 2017. The global decline of cheetah Acinonyx jubatus and what it means for conservation. *Proc. Natl Acad. Sci.* **114**, 528–533.

Duro, D. C., N. C. Coops, M. A. Wulder, and T. Han. 2007. Development of a large area biodiversity monitoring system driven by remote sensing. *Prog. Phys. Geog.: Earth Environ.* **31**, 235–260.

Eggen, M., M. Ozdogan, B. Zaitchik, and B. Simane. 2016. Land cover classification in complex and fragmented agricultural landscapes of the Ethiopian highlands. *Remote Sens.* **8**, 1020.

Frison, P. L., and E. Mougin. 1996. Monitoring global vegetation dynamics with ERS-1 wind scatterometer data. *Int. J. Remote Sens.* **17**, 3201–3218.

GDAL/OGR contributors. 2018. GDAL/OGR Geospatial Data Abstraction software Library. Open Source Geospatial Foundation.

Gómez, C., J. C. White, and M. A. Wulder. 2016. Optical remotely sensed time series data for land cover classification: a review. *ISPRS J. Photogramm. Remote Sens.* **116**, 55–72.

Gorelick, N., M. Hancher, M. Dixon, S. Ilyushchenko, D. Thau, and R. Moore. 2017. Google earth engine: planetary-scale geospatial analysis for everyone. *Remote Sens. Environ.* **202**, 18–27.

Grizonnet, M., J. Michel, V. Poughon, J. Inglada, M. Savinaud, and R. Cresson. 2017. Orfeo ToolBox: open source processing of remote sensing images. *Open Geospatial Data Soft. Stand.* **2**, 15.

Hagolle, O., M. Huc, D. Villa Pascual, and G. Dedieu. 2010. A multi-temporal method for cloud detection, applied to FORMOSAT-2, VENuS, LANDSAT and SENTINEL-2 images. *Remote Sens. Environ.* **114**, 1747–1755.

Hagolle, O., M. Huc, C. Desjardins, S. Auer, and R. Richter. 2017. MAJA Algorithm Theoretical Basis Document.

Henschel, P., L. Coad, C. Burton, B. Chataigner, A. Dunn, D. MacDonald, et al. 2014. The lion in West Africa is critically endangered. *PLoS ONE* **9**, 1–11.

Hirschmugl, M., C. Sobe, J. Deutscher, and M. Schardt. 2018. Combined use of optical and synthetic aperture radar data for REDD+ applications in Malawi. *Land* **7**, 116.

Inglada, J., A. Vincent, M. Arias, B. Tardy, D. Morin, and I. Rodes. 2017. Operational high resolution land cover map production at the country scale using satellite image time series. *Remote Sens.* **9**, 95.

Inoue, Y., T. Kurosu, H. Maeno, S. Uratsuka, T. Kozu, K. Dabrowska-Zielinska, et al. 2002. Season-long daily measurements of multifrequency (ka, ku, x, c, and l) and full-polarization backscatter signatures over paddy rice field and their relationship with biological variables. *Remote Sens. Environ.* **81**, 194–204.

Jones, E., T. Oliphant, and P. Peterson. 2001. SciPy: open source scientific tools for Python.

Joshi, N., M. Baumann, A. Ehammer, R. Fensholt, K. Grogan, P. Hostert, et al. 2016. A review of the application of optical and radar remote sensing data fusion to land use mapping and monitoring. *Remote Sens.* **8**, 70.

Kuenzer, C., M. Ottinger, M. Wegmann, H. Guo, C. Wang, J. Zhang, et al. 2014. Earth observation satellite sensors for biodiversity monitoring: potentials and bottlenecks. *Int. J. Remote Sens.* **35**, 6599–6647.

Lambin, E. F., and M. Linderman. 2006. Time series of remote sensing data for land change science. *IEEE Trans. Geosci. Remote Sens.* **44**, 1926–1928.

Laur, H., P. Bally, P. Meadows, J. Sanchez, B. Schaettler, E. Lopinto, et al. 2004. Derivation of the backscattering coefficient σ in ESA ERS SAR PRI products. Calibration/Validation Document Issue 2, Rev. 5f, ESA.

Lee, J.-S., M. R. Grunes, and E. Pottier. 2001. Quantitative comparison of classification capability: fully polarimetric versus dual and single-polarization SAR. *IEEE Trans. Geosci. Remote Sens.* **9**, 2343–2351.

Li, G., D. Lu, E. Moran, and S. Hetrick. 2011. Land-cover classification in a moist tropical region of Brazil with Landsat thematic mapper imagery. *Int. J. Remote Sens.* **32**, 8207–8230 PMID: 22368311.

Mairota, P., B. Cafarelli, R. K. Didham, F. P. Lovergine, R. M. Lucas, H. Nagendra, et al. 2015. Challenges and opportunities in harnessing satellite remote-sensing for biodiversity monitoring. *Ecol. Inform.* **30**, 207–214.

Mathieu, R., L. Naidoo, M. A. Cho, B. Leblon, R. Main, K. Wessels, et al. 2013. Toward structural assessment of semi-arid African savannahs and woodlands: the potential of multitemporal polarimetric RADARSAT-2 fine beam images. *Remote Sens. Environ.* **138**, 215–231.

McNairn, H., C. Champagne, J. Shang, D. Holmstrom, and G. Reichert. 2009a. Integration of optical and Synthetic Aperture Radar (SAR) imagery for delivering operational annual crop inventories. *ISPRS J. Photogramm. Remote Sens.* **64**, 434–449. Theme Issue: Mapping with SAR: Techniques and Applications.

McNairn, H., J. Shang, X. Jiao, and C. Champagne. 2009b. The contribution of ALOS PALSAR multipolarization and polarimetric data to crop classification. *IEEE Trans. Geosci. Remote Sens.* **47**, 3981–3992.

McNairn, H., A. Kross, D. Lapen, R. Caves, and J. Shang. 2014. Early season monitoring of corn and soybeans with TerraSAR-X and RADARSAT-2. *Int. J. Appl. Earth Obs. Geoinf.* **28**, 252–259.

Müller, H., P. Rufin, P. Griffiths, A. J. B. Siqueira, and P. Hostert. 2015. Mining dense Landsat time series for separating cropland and pasture in a heterogeneous Brazilian savanna landscape. *Remote Sens. Environ.* **156**, 490–499.

Nagendra, H. 2001. Using remote sensing to assess biodiversity. *Int. J. Remote Sens.* **22**, 2377–2400.

Naidoo, L., R. Mathieu, R. Main, K. Wessels, and G. P. Asner.2016. L-band synthetic aperture radar imagery performs better than optical datasets at retrieving woody fractional cover in deciduous, dry savannahs. *Int J Appl Earth Obs Geoinf.* **52**, 54–64.

Pelletier, C., S. Valero, J. Inglada, N. Champion, and G. Dedieu. 2016. Assessing the robustness of random forests to map land cover with high resolution satellite image time series over large areas. *Remote Sens. Environ.* **187**, 156–168.

Peterson, B., and K. J. Nelson. 2014. Mapping forest height in Alaska using GLAS, Landsat composites, and airborne LiDAR. *Remote Sens.* **6**, 12409–12426.

Pettorelli, N. 2013. *The normalized difference vegetation index*. OUP Oxford, Oxford.

Pohl, C., and J. L. V. Genderen. 1998. Review article multisensor image fusion in remote sensing: concepts, methods and applications. *Int. J. Remote Sens.* **19**, 823–854.

Quegan, S., and J. J. Yu. 2001. Filtering of multichannel SAR images. *IEEE Trans. Geosci. Remote Sens.* **39**, 2373–2379.

Rufin, P., D. Frantz, S. Ernst, A. Rabe, P. Griffiths, M. Özdoğan, et al. 2019. Mapping cropping practices on a national scale using intra-annual Landsat time series binning. *Remote Sens.* **11**, 232.

Sasaki, Y. 2007. The truth of the F-measure. *Teach Tutor mater* **1**, 1–5.

Schulte to Bühne, H., and N. Pettorelli. 2018. Better together: integrating and fusing multispectral and radar satellite imagery to inform biodiversity monitoring, ecological research and conservation science. *Methods Ecol. Evol.*, **9**:849–865.

Schwieder, M., P. J. Leitão, M. M. da Cunha Bustamante, L. G. Ferreira, A. Rabe, and P. Hostert. 2016. Mapping Brazilian savanna vegetation gradients with Landsat time series. *Int. J. Appl. Earth Obs. Geoinf.* **52**, 361–370.

Skidmore, A. K., N. Pettorelli, N. C. Coops, G. N. Geller, M. Hansen, R. Lucas, et al. 2015. Environmental science: agree on biodiversity metrics to track from space. *Nature* **523**, 403.

Small, D., and A. Schubert. 2008. Guide to ASAR geocoding. ESA-ESRIN Technical Note RSL-ASAR-GC-AD, 1.

Solbrig, O. T. 1996. Pp. 1–27*The Diversity of the Savanna Ecosystem*. Springer, Berlin Heidelberg, Berlin, Heidelberg.

Stefanski, J., T. Kuemmerle, O. Chaskovskyy, P. Griffiths, V. Havryluk, J. Knorn, et al. 2014. Mapping land management regimes in western Ukraine using optical and SAR data. *Remote Sens.* **6**, 5279–5305.

Symeonakis, E., T. Higginbottom, K. Petroulaki, and A. Rabe. 2018. Optimisation of savannah land cover characterisation with optical and SAR data. *Remote Sens.* **10**, 499.

Syrris, V., C. Corbane, M. Pesaresi, and P. Soille. 2019. Mosaicking Copernicus Sentinel-1 data at global scale. IEEE Transactions on Big Data, pages 1–1.

Trouve, E., Y. Chambenoit, N. Classeau, and P. Bolon. 2003. Statistical and operational performance assessment of multitemporal SAR image filtering. *IEEE Trans. Geosci. Remote Sens.* **41**, 2519–2530.

White, J. C., M. A. Wulder, G. W. Hobart, J. E. Luther, T. Hermosilla, P. Griffiths, et al. 2014. Pixel-based image compositing for large-area dense time series applications and science. *Can. J. Remote. Sens.* **40**, 192–212.

Wilcoxon, F. 1945. Individual comparisons by ranking methods. *Biometrics Bull.* **1**, 80–83.

Zhang, J. 2010. Multi-source remote sensing data fusion: status and trends. *Int. J. Image Data Fusion* **1**, 5–24.

Zhu, L., and R. Tateishi. 2006. Fusion of multisensor multitemporal satellite data for land cover mapping. *Int. J. Remote Sens.* **27**, 903–918.

Supporting Information

Additional supporting information may be found online in the Supporting Information section at the end of the article.

Figure S1. Boxplots of *F*-score distribution over the 20 classifications using hypertemporal time series with different inputs (S2_4: Sentinel-2 four bands, S2_10: Sentinel-2 ten bands, S2_4-NDVI: Sentinel-2 four bands and NDVI, S1: Sentinel-1 two polarizations and their ratio, S2_4-S1: S2_4 stacked with S1, S2_10-S1: S2_10 stacked with S1). **Figure S2.** Average *F*-score value over the 20 repetitions depending on the number of dates when using Sentinel-2 data (four or ten bands). **Table S1.** Absolute value of *Z*-statistics of the Wilcoxon test run between each pair of 20 *F*-score resulting from classifications using hypertemporal data. * means test is significant with *P*-value < 5%, **means test is significant with *P*-value < 1%. **Table S2.** Normalized (per row) confusion matrix of the classification reaching the highest *F*-score using Sentinel-2 and Sentinel-1 hypertemporal time series (input S2_10-S1, *F*-score = 81.4%). **Table S3.** Average *F*-score per class (%) over the 20 classifications using hypertemporal time series. **Table S4.** Average *F*-score per class (%) over the 20 classifications using Sentinel-2 data with different number of dates.

